The published version of the paper "Venturi S., Di Francesco S., Geier M., Manciola P. (2020). A new collision operator for lattice Boltzmann shallow water model: a convergence and stability study. Advances in Water Resources, 135, 103474." is available at: https://doi.org/10.1016/j.advwatres.2019.103474

Received ; | Revised ; | Accepted

DOI: xxx/xxxx

RESEARCH ARTICLE

A new collision operator for lattice Boltzmann shallow water model: a convergence and stability study

Sara Venturi[1] | Silvia Di Francesco[2] | Martin Geier[3] | Piergiorgio Manciola[1]

[1]University of Perugia, Civil and Environmental Department, Via G. Duranti 93, Perugia, Italy
[2]Niccolò Cusano University, Via Don Carlo Gnocchi, 3, Roma, Italy
[3]TU Braunschweig, Institute for Computational Modeling in Civil Engineering (iRMB), Braunschweig, Germany

Correspondence
Sara Venturi. Email: sara.venturi@unifi.it;
Silvia Di Francesco. Email: silvia.difrancesco@unicusano.it

Summary

This work presents a new lattice Boltzmann model for steady and unsteady two-dimensional shallow water flows. Compared to previous lattice Boltzmann based shallow water models, the proposed method uses a consistent characteristic speed in the pressure term and in the viscosity. To preserve the isotropy of viscosity, the relaxation rates for the different cumulants have to be decoupled. This is only possible by using multiple relaxation rates. The recovery of the correct viscosity is investigated by a convergence study based on the decay of a Taylor Green Vortex. Results from shallow water models using the proposed collision operator are then compared to those derived from standard BGK approach and from a continuous model.

KEYWORDS:
shallow water, collision operator, cumulant, convergence

1 | INTRODUCTION

The lattice Boltzmann method (LBM) is a mesoscopic method closely related to kinetic theory of gases. It is a versatile method and it has been extensively applied in different fields, such as turbulent flow[1,2], multiphase[3,4], flow in complex geometries[5,6], in porous media[7] and thermal flows[8]. However, it is not so common to use the LBM approach to simulate large scale hydraulic problems such as flooding events[9], dam breaks[10] and propagation of tsunamis. The LBM applies a stream and collide algorithm in which particles move on a Cartesian lattice and collide at lattice nodes. Once an appropriate lattice or velocity set has been chosen, the physics have to be implemented in the collision operator (CO) which is the central part of the model. A widespread solution is based on a single relaxation time (SRT) approach (BGK method[11]), characterized by a relatively simple implementation: the particle distribution relaxes towards an equilibrium function with a rate chosen to match the viscosity of the modeled fluid. In order to maximize the number of adjustable parameters and increase both stability and accuracy, some authors suggest to use a multiple relaxation times (MRT) CO[12]. Even though it was demonstrated that the MRT CO improves the stability range of the LBM, it introduces an additional Galilean invariance violation and hyper-viscosity problems when compared to the BGK CO[13]. The first problem is due to the definition of the moments. In fact, the MRT method translates the PDF into a set of raw moments[13] using a linear transformation. Each moment is orthogonal to all the others and relaxes with its own rate. However, the orthogonality of the moments is not reference frame independent[14] and orthogonality is not maintained if the reference frame is changed. Therefore, the original MRT method further violates the Galilean invariance, compared to a BGK-SRT model. By applying the collision in terms of cumulants instead of raw moments, the cumulant LBM[15] overcomes the violation of Galilean invariance, removing also the hyper-viscosity that can be generated using, for example, central moments in the collision operator[13]. Thus, in this work, we adopt the cumulant collision operator for the simulation of the shallow water equations in order to apply the LBM kinetic approach to large scale hydraulic problems and to increase stability and accuracy in the solution of the fluid dynamic problem.

The shallow water equations (SWE) are obtained from the Navier-Stokes equations by integrating over the water column from the ground to the free surface and assuming that the pressure along the vertical can be replaced by the hydrostatic pressure. They have been extensively applied to the simulation of large scale hydraulic problems using standard numerical methods[16]. The SWE were first studied with the LBM by Salmon[17] and Dellar[18], while Zhou provided a comprehensive revision of the method[19]. Thought some works presenting simulations of large scale problems[20,21,22] are available in literature, the issue of the effective applicability of a shallow water lattice Boltzmann model to complex hydraulic problems remains substantially open in term of efficiency, stability and accuracy. Most of the applications of the LBM for shallow water flows are based on the standard BGK approach[23] and only a small number of authors[24,25,26] applied multiple relaxation time collision operators to the problem. The objective of this work is to test the shallow water model using a non-conventional MRT collision operator and compare it to the standard BGK approach. In this work, a new model, based on cumulants, is originally described and its principal and innovative features and the main theoretical differences to the standard BGK are underlined. In order to retain the characteristics of the isotropy of the model, the equilibrium cumulants and corresponding relaxation rates are here defined and mathematically derived, taking into account the dependence of the characteristic speed on the water depth.
The paper is organized as follows: section 2 is a short introduction to the governing shallow water equations and lattice Boltzmann shallow water models; in particular, section 2.1 provides information on the LB models solving shallow water equations, with the description of the different COs and section 2.3 gives an extensive description of the cumulant model and its implementation procedure. Numerical results and model performance are presented in section 3. In particular, a comparison between the BGK model and the cumulant model is performed and the main differences are investigated. Especially, in section 3.4 and section 3.5, the test case of the Stoker dam break and the Fennema-Chaudhry dam break are used to show the different stability characteristics of the BGK and the innovative approach. Finally, section 4 presents conclusions.

2 | METHODS

The SWE are derived from the three dimensional incompressible Navier-Stokes equations. They are valid for problems in which the vertical dynamics of the fluid can be neglected[27]. In particular, the SWE are derived using an integration over the depth in order to obtain vertically averaged quantities. The pressure distribution in the vertical direction z, $p'(z)$, is supposed to be hydrostatic:

$$\frac{\partial p'}{\partial z} = -\rho' g' \tag{1}$$

where ρ' is the fluid (water) density and g' is the gravity acceleration. The superscript $'$ indicates physical variables, to distinguish them from variables in lattice units (l.u.). A system of 2D shallow water equations as in[19] can be written in the following form:

$$\frac{\partial h'}{\partial t} + \frac{\partial (h' u'_j)}{\partial x_j} = 0 \tag{2}$$

$$u'_j = \frac{1}{h'} \int_{z'_b}^{z'_b + h'} u' \, dz \tag{3}$$

$$\frac{\partial (h' u'_i)}{\partial t} + \frac{\partial (h' u'_i u'_j)}{\partial x_j} = -g' \frac{\partial}{\partial x_i} \left(\frac{h'^2}{2} \right) + \nu' \frac{\partial^2 (h' u'_i)}{\partial x_j \partial x_j} + F'_i \tag{4}$$

where i and j indicate the coordinate axis direction in 2D space, h' is the water depth, u' is the velocity, ν' is the kinematic viscosity, z_b is the bed elevation, F'_i is the external force in the i direction. The external force term can be written as follows:

$$F'_i = F'_{Pi} + F'_{si} + F'_{wi} + F'_{Ci} \tag{5}$$

where F'_{Pi} is the force due to gravity and is equal to $-g' h' \frac{\partial z_b}{\partial x_i}$; F'_{si} is the bed shear stress defined as:

$$F'_{si} = C_b u'_i \sqrt{u'_i u'_i} \tag{6}$$

where $C_b = g' \frac{n'^2_f}{h'^{1/3}}$ represents the friction factor with Manning's coefficient n'_f at the seabed. The terms F'_{wi} and F'_{Ci} are, respectively, the wind shear stress and the force representing the Coriolis effect.

In this work shallow water flows are modeled using a mesoscopic approach for the tracking of free surface dynamics. Flow characteristics are described by the evolution of a particle distribution function $f(x,t)$ (PDF) on a regularly spaced domain (lattice pattern), using the discrete Lattice Boltzmann equation:

$$f_\alpha\left(x + e_a\Delta t, t + \Delta t\right) = f_\alpha(x,t) + \Omega_\alpha + F_\alpha \qquad \alpha = 1, ..., m \tag{7}$$

where x is the position of the particle in the discretized space at time t, $f_\alpha(x,t)$ and e_α are the particle distribution functions and the set of discrete speeds along the m allowed lattice directions. The key steps in LBM are streaming and collision. In equation 7, $f_\alpha\left(x + e_a\Delta t, t + \Delta t\right) - f_\alpha(x,t))$ represents the streaming process and Ω_α is the collision operator; F_α represents the external forces.

The lattice pattern (DnQm - Dn stands for "n dimensions", while Qm stands for "m speeds") in LBM has the two functions to represent the points of the grid and to determine the particle directions of the motion. In the present work we adopt the D2Q9 pattern, with the following set of velocities $e_\alpha, (\alpha = 0, ..., 8)$[28]:

$$e_0 = \begin{pmatrix}0\\0\end{pmatrix} \quad e_1 = \begin{pmatrix}1\\0\end{pmatrix} \quad e_2 = \begin{pmatrix}0\\1\end{pmatrix} \quad e_3 = \begin{pmatrix}-1\\0\end{pmatrix} \quad e_4 = \begin{pmatrix}0\\-1\end{pmatrix}$$
$$e_5 = \begin{pmatrix}1\\1\end{pmatrix} \quad e_6 = \begin{pmatrix}-1\\1\end{pmatrix} \quad e_7 = \begin{pmatrix}-1\\-1\end{pmatrix} \quad e_8 = \begin{pmatrix}1\\-1\end{pmatrix}$$

In LBM, the macroscopic properties of the fluid can be expressed using the raw moments of the distribution. The generic raw moment $m_{\alpha\beta}$ can be expressed as:

$$m_{\alpha\beta} = \sum_{i,j} i^\alpha j^\beta f_{ij} \qquad i, j = -1, 0, 1 \tag{8}$$

where the sum of α and β indices represents the moment order. The indices i and j represent the Miller indices and, following a method primarily used in crystallography[29], allow to express speeds directions.

2.1 | Lattice Boltzmann shallow water model

In isothermal lattice Boltzmann models the characteristic speed is a parameter set to a constant that maximizes isotropy. The characteristic speed is usually identified with the speed of sound. For the D2Q9 lattice the speed of sound is equal to $c_s = \sqrt{1/3}$ lattice units. This fixed characteristic speed is an important simplification of the lattice Boltzmann method as it eliminates the need to fully resolve the energy flux tensor in velocity space[30]. To understand this point, we have to recall that the momentum distribution gives rise to an infinite hierarchy of moment equations. Due to the limited number of lattice velocities, only very few of these moment equations are independent of each other. On the D2Q9 lattice the moments m_{30} and m_{03} are not independently adjustable quantities. Physically they are part of the heat flux tensor. The trick applied in the lattice Boltzmann method to avoid a larger set of discrete velocities in which these moments were independent, is to chose a specific temperature (and hence characteristic speed) for which the moments m_{30} and m_{03} recover their correct physical value. This is only the case for $c_s = \sqrt{1/3}$ which explains why this constant characteristic speed is chosen. A detailed mathematical derivation is found in Appendix H of[13].

In the SWE the speed of surface waves takes the place of the speed of sound (characteristic speed) in the original LBM. In fact, in lattice Boltzmann shallow water (LB SW) models, the characteristic speed c_s is not constant but a function of the fluid elevation h and the gravity acceleration g:

$$c_s^2 = \frac{gh}{2} \tag{9}$$

This is a direct consequence of the equation of state $P = \frac{1}{2}gh^2$[18], where P indicates the macroscopic value of the pressure.

This poses a problem to the applicability of the LBM to the SWE. As the characteristic speed is no longer constant, the errors in the discretization of the third order moments do no longer cancel automatically[30]. This is important as the characteristic speed influences the viscosity. In fact, the kinematic viscosity (transport coefficient) of the fluid ν is linked to the relaxation rate ω and to the characteristic speed:

$$\nu = c_s^2\left(\frac{1}{\omega} - \frac{1}{2}\right) \tag{10}$$

The macroscopic properties (water depth h and velocity field u_i) of the flow are computed from the raw moments m_{00}, m_{10}/m_{01}, respectively.

$$h = \sum_{\alpha=0}^{8} f_\alpha \quad u_i = \frac{1}{h}\sum_{\alpha=0}^{8} e_{\alpha i} f_\alpha \quad \alpha = 0, ..., 8 \tag{11}$$

During the collision, update rules are applied at each node, depending only on the state of the PDF on the node. The collision has to conserve mass and momentum such that m_{00}, m_{10} and m_{01} are quantities that do not change during this step.

2.1.1 | From lattice units to physical units

In LB simulations, the grid spacing Δx and the elementary lattice time step Δt are linked through the physical value of the characteristic speed: $C_s = c_s \frac{\Delta x}{\Delta t}$. Then:

$$\Delta t = \frac{c_s}{C_s} \Delta x \qquad (s)$$

As reported in [28], the characteristic speed represents the velocity at which the waves travel.
Recalling that in SWE LBM the characteristic speed is defined as in equation (9), it follows that the value of the lattice time step Δt (in seconds s) is given by:

$$\Delta t = \left(\sqrt{gh/2} / \sqrt{g' h'/2} \right) \Delta x$$

where g and g' are the value of the gravity acceleration in lattice and physical units, respectively. In the practical implementation, h' can be maintained equal to h, then the expression of the lattice time step Δt becomes:

$$\Delta t = \sqrt{\frac{g}{g'}} \Delta x \quad (s) \tag{12}$$

The Froude number (Fr) of the physical model matches the lattice one:

$$Fr' = \frac{V'}{\sqrt{g' h'}} = \frac{V \frac{\Delta x}{\Delta t}}{\sqrt{g \frac{\Delta x}{\Delta t^2} h \Delta x}} = \frac{V \frac{\Delta x}{\Delta t}}{\frac{\Delta x}{\Delta t} \sqrt{gh}} = Fr \tag{13}$$

2.2 | Single relaxation time models

SRT models solving the shallow water equations are generally based on a BGK CO [17 19], assuming that collision is the process that returns particles to the state of the local Maxwellian equilibrium:

$$\Omega_\alpha = \frac{f_\alpha - f_\alpha^{eq}}{\tau} \tag{14}$$

where Ω_α is the collision operator and τ is the collision mean free time. Authors dealing with the solution of the shallow water equations using the BGK approach [31 32] suggest to express the equilibrium PDF as a power series in macroscopic velocities up to second order, assuring mass and momentum conservation:

$$f_\alpha^{eq} = \begin{cases} h - \frac{5gh^2}{6} - \frac{2h}{3} \mathbf{u} \cdot \mathbf{u} & \alpha = 0 \\ \beta h \left(\frac{gh}{6} + \frac{1}{3} \left(e_\alpha \cdot \mathbf{u} \right) + \frac{1}{2} \left(e_\alpha \cdot \mathbf{u} \right)^2 - \frac{1}{6} \mathbf{u} \cdot \mathbf{u} \right) & \alpha = 1, ..., 8 \end{cases} \tag{15}$$

where $\mathbf{u} = [u, v]$ with u and v that represent the velocity components; β assumes the value 1 if $\alpha = 1, ..., 4$ and $\frac{1}{4}$ otherwise [26].
In the D2Q9 model, the relation (8) implies there are only nine independent moments and, in particular $m_{30} = m_{10}$. In the SRT shallow water model (BGK SW) the characteristic speed is decoupled from the third order moment m_{30}: the model uses a c_s^2 different from $\frac{gh}{2}$ in the diffusion process. This can be evinced by observing the equilibrium equations used: the part related to the viscosity appears equal to the one adopted in a standard two dimensional LB model, while the part related to the density is different and takes into account the dependency of the characteristic speed c_s^2 on the depth of the water h (equation 15).
One of the properties of these models is therefore the decoupling of the viscosity from the characteristic speed to assure isotropy. In the next paragraph we propose and derive the cumulant collision operator where the physical link between the characteristic speed and viscosity is maintained and the isotropy of the viscosity is restored by applying different relaxation rates to different second order cumulants.

2.3 | Cumulant model

While the original MRT model performs collision on moments, the cumulant model (CumLB) performs the collision on cumulants. Cumulants quantify the deviation of a distribution from a Gaussian distribution. By design cumulants are statistically

independent of each other. Cumulants are conveniently obtained from central moments, defined as:

$$\kappa_{\alpha\beta} = \sum_{i,j} (i-u)^{\alpha}(j-v)^{\beta} f_{ij} \qquad i,j = -1,0,1 \tag{16}$$

where the subscripts i and j indicate the corresponding components of the speed vectors of the PDF.
For the D2Q9 pattern used in this work, all but one of the available cumulants are identical to the corresponding central moments. In particular:

$$\begin{cases} C_{00} = \kappa_{00} \\ C_{10} = \kappa_{10} \\ C_{01} = \kappa_{01} \\ C_{20} = \kappa_{20} \\ C_{02} = \kappa_{02} \\ C_{11} = \kappa_{11} \\ C_{12} = \kappa_{12} \\ C_{21} = \kappa_{21} \end{cases} \tag{17}$$

Starting from fourth order, cumulants differ from central moments[13]. The D2Q9 pattern, used in this work, has only one independent fourth order cumulant:

$$C_{22} = \kappa_{22} - \left(\kappa_{20}\,\kappa_{02} + 2{\kappa_{11}}^2\right)/h \tag{18}$$

Then, equilibrium cumulants are identical to equilibrium central moments[15] except for the fourth order cumulant that is zero. The equilibrium cumulants for a D2Q9 scheme are given by:

$$\begin{cases} C_{00} = h \\ C_{10} = 0 \\ C_{01} = 0 \\ C_{20} = c_s^2 h \\ C_{02} = c_s^2 h \\ C_{11} = 0 \\ C_{12} = 0 \\ C_{21} = 0 \\ C_{22} = 0 \end{cases} \tag{19}$$

The CumLB method is implemented by transforming the distributions to cumulants before the collision using the following equations:

$$\begin{cases}
\kappa_{00} = f_7 + f_3 + f_6 + f_4 + f_0 + f_2 + f_8 + f_1 + f_5 \\
\kappa_{10} = 0 \\
\kappa_{01} = 0 \\
\kappa_{20} = (-1-u)^2 f_7 + (-1-u)^2 f_3 + (-1-u)^2 f_6 + u^2 f_4 + u^2 f_0 + u^2 f_2 + (1-u)^2 f_8 + (1-u)^2 f_1 + (1-u)^2 f_5 \\
\kappa_{02} = (-1-v)^2 f_7 + v^2 f_3 + (1-v)^2 f_6 + (-1-v)^2 f_4 + v^2 f_0 + (1-v)^2 f_2 + (-1-v)^2 f_8 + v^2 f_1 + (1-v)^2 f_5 \\
\kappa_{11} = (-1-u)(-1-v) f_7 - (-1-u) v f_3 + (-1-u)(1-v) f_6 + -u(-1-v) f_4 + uv f_0 - u(1-v) f_2 + (1-u)(-1-v) f_8 + \\
-(1-u) v f_1 + (1-u)(1-v) f_5 \\
\kappa_{21} = (-1-u)^2(-1-v) f_7 - (-1-u)^2 v f_3 + (-1-u)^2(1-v) f_6 + +u^2(-1-v) f_4 - u^2 v f_0 + u^2(1-v) f_2 + (1-u)^2(-1-v) f_8 \\
-(1-u)^2 v f_1 + (1-u)^2(1-v) f_5 \\
\kappa_{12} = (-1-u)(-1-v)^2 f_7 + (-1-u) v^2 f_3 + (-1-u)(1-v)^2 f_6 - u(-1-v)^2 f_4 - u v^2 f_0 - u(1-v)^2 f_2 \\
+(1-u)(-1-v)^2 f_8 + (1-u) v^2 f_1 + (1-u)(1-v)^2 f_5 \\
\kappa_{22} = (-1-u)^2(-1-v)^2 f_7 + (-1-u)^2 v^2 f_3 + (-1-u)^2(1-v)^2 f_6 + u^2(-1-v)^2 f_4 + u^2 v^2 f_0 \\
+u^2(1-v)^2 f_2 + (1-u)^2(-1-v)^2 f_8 + (1-u)^2 v^2 f_1 + (1-u)^2(1-v)^2 f_5
\end{cases} \tag{20}$$

In the collision step, cumulants are relaxed following the equations:

$$C^{pc}_{\alpha\beta} = C_{\alpha\beta} - \omega_{\alpha\beta}\left(C_{\alpha\beta} - C^{eq}_{\alpha\beta}\right) \tag{21}$$

where $C^{eq}_{\alpha\beta}$ is the equilibrium cumulant and $C^{pc}_{\alpha\beta}$ is the post-collision one. A cumulant related to the definition of the value of the transport coefficient ν is C_{11}, while the corresponding cumulants obtained from the rotational invariance constraint[15] are C_{20} and C_{02}. Then, in order to retain the isotropy of the model, the latter cumulants are relaxed together:

$$\begin{cases}
C^{pc}_{20+02} = C_{20+02} - \omega_{20+02}\left(C_{20} - C^{eq}_{20} + C_{02} - C^{eq}_{02}\right) \\
C^{pc}_{20-02} = C_{20-02}\left(1 - \omega_{20-02}\right)
\end{cases} \tag{22}$$

with $C_{20+02} = C_{20} + C_{02}$ and $C_{20-02} = C_{20}$ - C_{02}. The relaxation rates related to the kinematic viscosity are ω_{11} and ω_{20-02}:

$$\omega_{11} = \frac{1}{3\nu + 0.5} \qquad \omega_{20-02} = \omega_{11} \tag{23}$$

with $\omega_{20-02} = \omega_{20}$ - ω_{02}. The only relaxation rates that influence the viscosity to leading order are ω_{11} and ω_{20-02}. The relaxation rate ω_{20+02} can be imposed equal to unity or related to the bulk viscosity. The remaining relaxation rates are free parameters and can be chosen in the range $\{0, ..., 2\}$ to improve stability or accuracy.

In section 3.3.5 we investigate some options for the choice of these relaxation rates. Finally, post collision cumulants are

transformed to distributions:

$$\begin{cases} f_0 = -\kappa_{20} + \kappa_{22} + 2\kappa_{12}u + \kappa_{02}(-1+u^2) + 2\kappa_{21}v + 4\kappa_{11}uv + \kappa_{20}v^2 + \kappa_{00}\left(-1+u^2\right)\left(-1+v^2\right) \\ f_1 = \frac{1}{2}\left(\kappa_{20} - \kappa_{22} + \kappa_{00}u - \kappa_{02}u + +\kappa_{00}u^2 - \kappa_{02}u^2 + -\kappa_{12}(1+2u) - 2\kappa_{11}v - 2\kappa_{21}v - 4\kappa_{11}uv - \kappa_{20}v^2 - \kappa_{00}uv^2 - \kappa_{00}u^2v^2\right) \\ f_2 = \frac{1}{2}\left(\kappa_{02} - \kappa_{22} - 2\kappa_{11}u - 2\kappa_{12}u + -\kappa_{02}u^2 + \kappa_{00}v - \kappa_{20}v - 4\kappa_{11}uv + -\kappa_{00}u^2v + \kappa_{00}v^2 - \kappa_{20}v^2 - \kappa_{00}u^2v^2 - \kappa_{21}(1+2v)\right) \\ f_3 = \frac{1}{2}\left(\kappa_{12} + \kappa_{20} - \kappa_{22} - \kappa_{00}u + \kappa_{02}u - 2\kappa_{12}u + \kappa_{00}u^2 + -\kappa_{02}u^2 + 2\kappa_{11}v - 2\kappa_{21}v - 4\kappa_{11}uv - \kappa_{20}v^2 + \kappa_{00}uv^2 - \kappa_{00}u^2v^2\right) \\ f_4 = \frac{1}{2}\left(\kappa_{02} + k21 - \kappa_{22} + 2\kappa_{11}u - 2\kappa_{12}u - \kappa_{02}u^2 - \kappa_{00}v + \kappa_{20}v - 2\kappa_{21}v + -4\kappa_{11}uv + \kappa_{00}u^2v + \kappa_{00}v^2 - \kappa_{20}v^2 - \kappa_{00}u^2v^2\right) \\ f_5 = \frac{1}{4}\left(\kappa_{12} + \kappa_{21} + \kappa_{22} + \kappa_{02}u + 2\kappa_{12}u + \kappa_{02}u^2 + \kappa_{20}v + 2\kappa_{21}v + +\kappa_{00}uv + \kappa_{00}u^2v + \kappa_{20}v^2 + \kappa_{00}uv^2 + \right. \\ \left. +\kappa_{00}u^2v^2 + \kappa_{11}(1+2u)(1+2v)\right) \\ f_6 = \frac{1}{4}\left(\kappa_{21} + \kappa_{22} - \kappa_{02}u + \kappa_{02}u^2 + \kappa_{12}(-1+2u) + \kappa_{20}v + 2\kappa_{21}v + -\kappa_{00}uv + \kappa_{00}u^2v + \kappa_{20}v^2 - \kappa_{00}uv^2 + \right. \\ \left. +\kappa_{00}u^2v^2 + \kappa_{11}(-1+2u)(1+2v)\right) \\ f_7 = \frac{1}{4}\left(-\kappa_{21} + \kappa_{22} - \kappa_{02}u + \kappa_{02}u^2 + \kappa_{12}(-1+2u) - \kappa_{20}v + +2\kappa_{21}v + \kappa_{00}uv - \kappa_{00}u^2v + \kappa_{20}v^2 - \kappa_{00}uv^2 + \right. \\ \left. +\kappa_{00}u^2v^2 + \kappa_{11}(-1+2u)(-1+2v)\right) \\ f_8 = \frac{1}{4}\left(\kappa_{12} - \kappa_{21} + \kappa_{22} + \kappa_{02}u + 2\kappa_{12}u + \kappa_{02}u^2 - \kappa_{20}v + 2\kappa 21v + -\kappa_{00}uv - \kappa_{00}u^2v + \kappa_{20}v^2 + \kappa_{00}uv^2 + \right. \\ \left. +\kappa_{00}u^2v^2 + \kappa_{11}(1+2u)(-1+2v)\right) \end{cases} \tag{24}$$

2.3.1 | Specific characteristics of cumulant CO based model

In the D2Q9 model, relation (8) implies there are only nine independent moments and, in particular:

$$m_{30} = m_{10} \tag{25}$$

The coincidence of higher order moments with lower order ones is known as aliasing. Referring to the theory of cumulants[13] or, similarly, to the Taylor expansion of the Maxwell-Boltzmann distribution up to second order in the Mach number[33], it can be shown that the third order equilibrium moment m_{30}^{eq} is equal to:

$$m_{30}^{eq} = \left(3 \cdot c_s^2 \cdot u + u^3\right) h \tag{26}$$

If the normalized value of m_{30}^{eq} is considered and the high order term u^3 is neglected, the moment m_{30}^{eq} becomes:

$$m_{30}^{eq} = 3 \cdot c_s^2 m_{10}^{eq} = 3 \cdot c_s^2 m_{30}^{eq} \tag{27}$$

This explains why, in an isothermal single phase lattice Boltzmann model, the characteristic speed is considered constant and equal to $\sqrt{\frac{1}{3}}$.

As already pointed out, the characteristic speed c_s in a shallow water LB model is not constant but variable with the depth of the water[18]. The relationship (25) is hence not fulfilled by a SWE LBM. All previous models solved this problem by decoupling the viscosity from the characteristic speed. In that way the equilibrium distribution function does no longer represent an approximation of the Maxwellian. In what follows we propose an alternative solution to the problem that respects the dependence of the viscosity on the characteristic speed and captures the first nine moments of the Maxwellian equilibrium exactly. Since the aliasing relation (25) can no longer be fulfilled, the isotropy of the viscosity has be restored by the use of different relaxation rates for the two moments controlling viscosity. Hence, the following strategy is adopted:

- the characteristic speed is assumed variable following equation (9)
- the expression of c_s^2 enters in the definition of cumulants of the equilibrium;
- in the collision step, the relaxation rate of 2^{nd} order cumulants are adjusted in order to retain the isotropy during the collision:

$$\omega_{11} = \left(\frac{2}{3gh}\left(\frac{1}{\omega} - \frac{1}{2}\right) + \frac{1}{2}\right)^{-1} \tag{28}$$

and

$$\omega_{20-02} = \left(\frac{\frac{2}{3}\left(\frac{1}{\omega} - \frac{1}{2}\right)}{1 - \frac{gh}{2}} + \frac{1}{2}\right)^{-1} \tag{29}$$

where the ω is related to the kinematic viscosity of the fluid (equation 10).

3 | RESULTS

3.1 | Convergence study in diffusive scaling

As the two possible strategies to solve the SWE with LBM differ in the way they impose an isotropic viscosity, we show here the performance of the respective models in recovering the target viscosity. To this end we conduct a convergence study (section 3.2 and 3.3) by measuring the error in *diffusive scaling*: the time step scales proportionally to the square of the grid spacing ($\Delta t \propto \Delta x^2$). The setting allows to maintain a constant value of Reynolds number at constant viscosity under grid refinement. The asymptotic behavior of the measured viscosity ν_m is determined by fitting the logarithm of the amplitude of a decaying wave to a linear function. The slope is related to the measured viscosity through the square of the wave vector. The normalized error of the viscosity $ER\nu$, with respect to the theoretical viscosity $\nu = c_s^2\left(\tau - \frac{1}{2}\right)\frac{\Delta x^2}{\Delta t}$ is defined as: $ER_\nu = |\nu_m - \nu|/\nu$.
The phase lag can be considered a measure of the level of Galilean invariance (GI) in the model. Thus the GI of the proposed method is investigated by calculating the phase lag ER_Φ every turn, when the wave comes back to its original position.

3.2 | Shear wave test

In the shear wave test, the asymptotic behavior in diffusive scaling ($\Delta t \propto \Delta x^2$) of a one dimensional decaying shear wave is investigated. The dimensions of the domain are $L\times3$ nodes, with L varying from 32 to 256 nodes. Periodic boundary conditions are used. The simulation was run for $20000\left(L/L_0\right)^2$ time steps and the wave amplitude was measured every $1000\left(L/L_0\right)^2$ time steps. In order to avoid any influence of the initial conditions on the asymptotic decay, the values of viscosity and phase were compared to the measurement obtained after $10000\left(L/L_0\right)^2$ time steps. The velocity is scaled with: $\left(\frac{L}{L_0}\right)$. The initial conditions are given by:

$$u(x, t=0) = u_0\frac{L_0}{L} \qquad v(x, t=0) = v_0\frac{L_0}{L}\sin\frac{2\pi x}{L}$$

with L_0=32, u_0=0.01 and v_0=0.1. All the quantities are expressed in lattice units (l.u.). The physical values are: $L_0\Delta x$, $u_0(\Delta x/\Delta t)$, $v_0\,(\Delta x/\Delta t)$, with $\Delta x = 1$m and Δt given by the relation (12).
The analytical solution of the problem is given by:

$$v(x,t) = v_0\frac{L_0}{L}\sin\frac{2\pi x}{L}e^{-\nu t\left(\frac{2\pi}{L}\right)^2}$$

Hereafter, the results of the CumLB and BGK SW are shown (Fig.1). The error in viscosity in the CumLB model is comparable with the ones of BGK SWE. For example, with $\nu = 0.01$ and $h = 1$, in the cumulant model the normalized error in viscosity is 0.00284 for $L = 32$ nodes and 0.0000443 for $L = 256$ nodes. In the BGK SW, it is generally slightly higher, 0.0029 for $L = 32$ nodes and 0.0000453 for $L = 256$ nodes. Moreover, all the models show a second order convergence with the increase of the resolution.
The error in phase (phase lag) is measured when the wave should have come back to its original position. The number of time steps after which the wave should return is equal to: $u_0 \cdot \frac{L_0}{L}$. The error in phase lag shows a fourth order accuracy. It should be clarified that a fourth order phase lag is due to the alignment of the wave with the grid and that, in general, the method is second order accurate[13]. The value of the phase lag is similar in CumLB and BGK SW model.

3.3 | Taylor Green Vortex test

Due to its simplicity in both initial and boundary conditions, the Taylor Green Vortex has been studied extensively and serves as a well-established reference and benchmark test problem for numerical simulation: it allows a straightforward validation of the code and is ideally suited for a structured grid approach[34]. The decay of a Taylor Green Vortex in a fully periodic domain is investigated, to assess the accuracy of the transport coefficient (viscosity) and the phase lag. Computations are performed considering a domain of variable length L and width W. Different scenarios are based on values of L equal to 32, 64, 128, 256 Δx, and width W equal to 48, 96, 192 and 384 Δx, respectively. The difference in the dimensions of the domain ($L \neq W$)

allows to check for possible defects in the isotropy of the model and for the presence of preferential directions.
At the beginning of the simulation, the values of the velocity along the x-axis and y-axis, and of water depth, are:

$$u(x, y, t = 0) = u_0 \frac{L_0}{L} - U \frac{L_0}{L} \sqrt{\frac{k_y}{k_x}} cos\left(k_x x\right) sin\left(k_y y\right) \tag{30}$$

$$v(x, y, t = 0) = U \frac{L_0}{L} \sqrt{\frac{k_x}{k_y}} sin\left(k_x x\right) cos\left(k_y y\right) \tag{31}$$

$$h(x, y, t = 0) = h_0 \left(1 - \frac{\left(U^2 \frac{L_0^2}{L^2}\right)}{4c_s^2} \left(\frac{k_y}{k_x} cos\left(2k_x x\right) + \frac{k_x}{k_y} sin\left(2k_y y\right) \right) \right) \tag{32}$$

having indicated with k_x and k_y, the components of the wave vectors :

$$k_x = \frac{2\pi}{L} \qquad k_y = \frac{4\pi}{3L} \qquad \frac{k_x}{k_y} = \frac{3}{2} \tag{33}$$

L_0 is set equal to 32, u_0 and U are chosen considering two different velocity configurations, namely "slow set" and "fast set". For the slow set : $u_0 = 0.01\frac{\Delta x}{\Delta t}$ and $U = 0.00035\frac{\Delta x}{\Delta t}$ while for the fast set $u_0 = 0.096\frac{\Delta x}{\Delta t}$ and $U = 0.0035\frac{\Delta x}{\Delta t}$. The value of the grid spacing is $\Delta x = 1$ m; the value of Δt is given by the equation (12).
The viscosity value is then defined as: $\nu = c_s^2 \left(\tau - \frac{1}{2}\right) \frac{\Delta x^2}{\Delta t}$. An analytical solution of the wave velocity along the y-axis is given by:

$$v(x, y, t) = U \frac{L_0}{L} \sqrt{\frac{k_x}{k_y}} sin\left(k_x x\right) cos\left(k_y y\right) e^{\frac{t}{t_D}} \tag{34}$$

where t_D (decay time of the wave) is equal to:

$$t_D = \frac{1}{\nu \left(k_x^2 + k_y^2\right)} \tag{35}$$

The aforementioned initial conditions are set as in [35], with the difference that our domain is not isotropic.
Simulations are run with viscosities $\nu = 0.01, 0.001, 0.0001$ and different depths $h = 1, 0.5, 0.1$.
The simulation setup uses the diffusive scaling. In such a way, velocities and times are always multiplied by the factor $\frac{L_0}{L}$ and $\left(\frac{L_0}{L}\right)^2$, respectively.

3.3.1 | Error in viscosity

The asymptotic behavior of the viscosity of the CumLB and BGK SWE has been compared for various values of viscosities ν and depths of the water h to take the variations in the characteristic speed into account. The logarithm of the normalized viscosity error is plotted against the logarithm of the number of nodes. For $h = 1$, the trend of the viscosity error slope is in between second and third order convergence for the CumLB model. In the cumulant model with slow velocity set and $\nu = 0.01$, the slope is $\cong -2.35$ (Fig. 2, case (a)) but it approaches -2 for lower values of h (Fig. 2, case (b) and case (c)).
If stable, the BGK SWE are always characterized by a slope trend equal to $\cong -2.0$.
First of all, it is noteworthy that the BGK SW model is characterized by a more limited range of stability. In fact, the BGK model becomes unstable for a value of h equal to 1.0 for all the considered viscosities, $\nu = 0.01, 0.001, 0.0001$ (Fig. 2 case (a), (d) and (g)). The BGK SW results are slightly more accurate than those of the CumLB model for low depths only if the slow velocity set is considered (i.e., Fig. 2 case (c), (h) and (i)). Conversely, for the fast velocity set, the CumLB model wins. For h=0.5, the CumLB model is more accurate with ν=0.01 and $\nu = 0.001$ (Fig. 2 case (b) and (e)), BGK with $\nu = 0.0001$ (Fig. 2 case (h)). Furthermore, it should be noted that, generally, in CumLB model the error in viscosity increases with the reduction of viscosity, as already discussed in [13]. On the other hand, the viscosity error in the BGK SWE changes in a limited manner with the reduction of viscosity.
As expected, simulations performed with a fast velocity set are characterized by some cases missing because of instability (Fig. 3), cases (d), (g) and (i) are missing); furthermore, all the models show a viscosity error much higher than for the slow velocity. For example, taking into consideration results of CumLB with $\nu = 0.01$ and $h = 1.0$, an increment in the fast set of translational

velocity u_0 and of the amplitude of the velocity of the wave U by a factor of about tenth leads to a forty times increase of the error (for comparison, Fig. 2 case (a) and Fig. 3 case (a)). Nevertheless, it has to be pointed out that, if the model remains stable, errors can be considered essentially low in all the cases, taking a maximum value of 0.015% for CumLB model and 0.02% for BGK SW, respectively.

3.3.2 | Phase lag measure

In all the models examined, the error in phase is defined by a slope of the trend equal to -2, as generally expected in lattice Boltzmann models. As already observed in the previous section 3.3.1, the instability that characterizes the BGK SW and starts from depths higher than 0.5, does not allow to measures the phase for $h = 1$ (cases (a), (d) and (g) of Fig. 4 and 5).
At slow velocities (Fig. 4), the error in phase of the CumLB model appears to be slightly influenced by the depth and viscosity values. In fact, it evidently (Fig. 4, case (a), (b) and (c)) increases if the depth decreases. For example, in a 256×384 nodes domain, the difference of the error for the viscosities $\nu = 0.01$ and $\nu = 0.0001$ is about 2.5% for h =1 and about 40% for h = 0.1. On the other hand, the BGK model is characterized by an error in phase less variable with depth and viscosity, as it was already observed in the section regarding the viscosity error (section 3.3.1).
For $h = 0.1$, viscosity $\nu = 0.0001$, $L = 32$ and $L = 32$, the cumulant model is not stable.
In all the models, the phase lag increases with the velocity (Fig. 5). For example, in the cumulant model, the error for the fast velocities set is about 0.5% ($h = 1$), 0.4% ($h = 0.5$) and 0.3% ($h = 0.1$) higher than for the slow set. The error was calculated considering the medium value for all the viscosities. In the BGK SW this difference is not seen and the phase lag grows by 0.5% for all the depths. It has to be pointed out that in BGK SW the error does not change significantly with the change in the viscosity value (for example, Fig. 5 case (b), (e) and (h)). If $h = 1$ and $\nu = 0.001$ (Fig. 5, case (d)), CumLB exhibits an higher accuracy in phase.

3.3.3 | Results for high viscosities

Results from the previous sections clearly exhibit the unstable behavior of BGK for h between 0.5 and 1, with all the viscosities taken into consideration. BGK returns to stable solutions for $\nu = 0.1$ and $h \geq 1$ (Fig. 7), maintaining the trend already observed in sections 3.3.1 and 3.3.2. In such a case, the cumulant model continues to display a stable behavior for a viscosity value $\nu = 0.1$ and $h \geq 1$ (Fig. 6). Analyzing the simulation results (not shown in this work), it was noted that the trend illustrated in the previous cases (Fig. 2, 3, 4, 5) was maintained; in fact, an accuracy decrease, both for BGK and CumLB, can be put in evidence adopting high viscosities. In the evaluation of the errors for viscosities higher than $\nu = 0.01$, a shorter time sampling of measurements has to be taken into consideration than for the lower viscosities, as the decay time drops exponentially with the viscosity. For a viscosity equal to ν=0.1, the sampling interval chosen is $100\left(\frac{L}{L_0}\right)^2$.

3.3.4 | Observations about stability range

In this work, a new MRT collision operator is presented and applied to the solution of shallow water equations. As a first result and validation, a study on accuracy and stability of the CumLB model against the standard BGK model is proposed and discussed. In particular, the Taylor Green Vortex test in a rectangular domain has been considered significant to evaluate the behavior of the models also from the point of view of isotropy as this flow has velocity components not aligned with any of the primary axes. In Fig. 6 and 7, the stability range of the models is shown. The stability range changes for the different values of depths of the water h and translational velocity u_0. To define the range of stability, an intermediate velocities value (between the fast and slow set) was considered with $u_0 = 0.05$ and wave amplitude $U = 0.00175$. Circles indicate the points where the simulation was performed. When stable, all models show a second order convergence in viscosity error and in phase error. The h characterized by the most stable behavior is 0.5. Here the simulations are stable for all the value of the viscosities taken into consideration. If the value of the depth moves towards lower or higher values, the stability properties change. In particular, for low depths (h = 0.1), both models are stable for the lowest viscosities ($\nu = 0.001$ and $\nu = 0.0001$) only if using low translational velocities. For depths going towards the value of 1.0, the CumLB model is always stable for the slow set of translational velocities. For the fast set, we have to arrive to a viscosity value equal to $\nu = 0.01$ to have a stable behavior.
It is clear from Fig. 6 and 7 that the CumLB model is characterized by a wider stability range. In fact, the BGK becomes unstable for h values between 0.5 and 1. Several areas are totally missing in the BGK stability range - graph. BGK starts to become stable again only for high viscosities ($\nu \geq 0.1$) and depths ($h \geq 1$).

3.3.5 | Choices of relaxation rates parameters

It needs to be clarified that all the results presented so far were obtained with the relaxation rates for the bulk mode, the third order and fourth order cumulant set to one. This choice is known to be particularly stable but it is also known that this is not the most accurate choice. Some particular combinations of relaxation rates can lead to drastic improvement of accuracy[36,37]. To investigate the effect of using different values of relaxation rates, two approaches were taken into consideration: under relaxation and over relaxation of third order cumulants. The under-relaxation of third order cumulants can be obtained by means of the Ginzburg coefficient. Ginzburg showed that by selecting an appropriate combination of the odd and even rates it was possible to obtain the correct solution for the Poiseuille and Couette flow test cases[38]. For the D2Q9 model, the Ginzburg coefficient becomes: $\Lambda = (1/\omega_{11} - 1/2) \cdot (1/\omega_{21} - 1/2)$. We selected the simple values Λ=1/4 and Λ=1/6. In the case of the Taylor Green Vortex test both values of Λ lead to a significant accuracy decrease in viscosity and in phase. Different results were achieved with the over-relaxation of third order cumulants. It can be obtained imposing $\omega_{21} = \omega_{11}$. In some cases, this choice of parameters gave better results than under-relaxation. For example, taking into account the error in phase (section 3.3.2), we have observed an improvement in accuracy. The best results are obtained for the highest viscosity (ν=0.01) and the lowest height (h=0.1). Considering the low velocity set, the improvement of the over-relaxation with respect to the case $\omega_{21} = 1$ is about 39 %. Considering the high velocity set, the improvement is about 32 %. However, the over-relaxed cumulant does not always enhance the accuracy in viscosity. A decisive improvement is only observed in a limited number of cases. Moreover, it was found that the effects of over-relaxation on stability are not always positive. In fact, despite a few cases where the stability improves for low heights, it becomes worse in particular for a range of heights between 0.5 and 1.

3.4 | Stoker dam break

One of the test cases of a dam break flow was given from Stoker[39] and it has become a standard benchmark for the shallow water equations[40]. Hereafter, the one - dimensional Stoker dam break is presented, in order to compare the BGK model with the new MRT model. The numerical results of the CumLB model are compared with the non - stationary analytical solution at a certain time. A fluid domain of 200 m × 200 m was taken into account. At the boundaries, no-slip is imposed (Figure 8, simulation setup). The bed is flat and frictionless. At t=0 the flow is at rest and characterized by two different water levels, h_l= 10 m and h_r= 5 m, with the presence of a step-wise discontinuity at x=100 m. The initial conditions are set to:

$$\begin{cases} u(x) = 0 \ \ m/s & everywhere \\ h_l = 10 \ \ m & 200m > x \geq 100m \\ h_r = 5 \ \ m & 100m > x \geq 0m \end{cases}$$

The instantaneous breach of the dam leads to a transient flow consisting of two waves. The one reflects from the discontinuity to the region with the higher water level. The other is a shock wave moving in the opposite direction. At time t = 6 s a sensitivity analysis for different grid spacings was carried out for the CumLB model. The relaxation rate τ was set to 0.85 and various Δx = 1, 0.5, 0.25 m were considered. In the flat regions a good agreement between the simulation and the analytical solution is observed. Due to numerical diffusion, the slopes are less well recovered but the agreement improves with higher resolution (Figure 8). It is also possible to note a slight oscillation at the shock front. This phenomenon, common in discrete approximations and analogous to Gibbs oscillations[41], is an obstacle to the stability of the LB schemes. The oscillation becomes stronger with lower viscosity. The Gibbs effect is highlighted in the following graphs where the trend of h and u is shown for different times: 2, 4, 6 and 8 s (Figure 9 and 10). The value of the relaxation rate is set to 0.6 which is lower than in previous case. Δx is set to 1 m. The oscillations are especially evident in the case of the BGK model. Due to the strong Gibbs oscillations, the BGK model becomes unstable before the end of the simulation at time t=15 s after the bounce back of the wave at the wall. We point out that the value of the grid spacing does not influence the extent of the oscillations. To further investigate the stability properties of the cumulant CO at different viscosities, we gradually decrease the value of τ and Δx. Results shows that, using a Δx =0.125 m, the simulation is still stable for τ=0.5001, corresponding to a physical viscosity $\nu = 5.05 \cdot 10^{-6} \ m^2/s$ which is close to the value of water. The threshold value of τ for BGK CO is 0.65 corresponding to $\nu = 7.5 \cdot 10^{-3} \ m^2/s$ which is three orders of magnitude higher than the one reached for the cumulant CO. Moreover, a lower value of τ corresponds to simulation results closer to the analytical solution with regard to the knees (Fig. 11).

3.5 | Asymmetrical dam break of Fennema-Chaudhry

The Fennema-Chaudhry dam break has been used extensively in literature as a test case for the shallow water equations[42]. The spatial domain is a 200 m × 200 m flat region without friction at the bed and a dam in the middle[16]. The numerical parameters of the simulation are Δx=0.1 m, Δt=0.0082 s and τ=0.7. At t=0, the level of the water surface is set 10 m for the upstream region and 5 m for the downstream region (Figure 12, simulation setup). The asymmetrical dam-break was simulated using the cumulant CO and the BGK SW model. The value of viscosity in this example is artificially increased and differs from that of water. This is due to the fact that the BGK CO is unstable for lower value of τ and a comparison of results is feasible only in the stability range of both investigated models. Moreover, outcomes were compared to results from a finite volume numerical model, RiverFlow 2D[43], that implements non-linear shallow water equations and is based on adaptive triangular meshes. The model solves mass and momentum conservation equations in a plane obtained by depth-averaging Navier-Stokes equations. As most of 2D models available in literature this model neglects the diffusion of momentum due to viscosity: $\upsilon \frac{\partial^2 (hu_i)}{\partial x_j \partial x_j}$. A comparison with the continuous model will be therefore only qualitative. As observed from figures 13 and 14, the BGK-SW model and the CumLB model show similar results and the agreement between these solutions and the RiverFlo 2D solution is satisfactory. The simulations with the cumulant and the BGK CO start to differ significantly from each other after the impact of the wave with the east wall. In fact, the CumLB model continues to exhibit a stable behavior at the impact (t=11.5 s), after the reflection of the wave (t=14 s) and at the impact with the dam (t=23.3 s) (figure 15), while the BGK-SW model becomes unstable. This is a further evidence of the stability improvement in lattice shallow water schemes due to the introduction of the cumulant CO. Figure 16 shows the good agreement between the water depth hydrographs of RiverFlow 2D model and CumLB model, at the two point P1 and P2 (figure 12) located at the middle of the breach.

4 | CONCLUSIONS

In this work an alternative approach to solve the shallow water equations with the Lattice Boltzmann model was proposed and investigated. All previous LBM SWE models used a decoupling of the viscosity from the characteristic speed to assure isotropy. In this work the physical link between the characteristic speed and viscosity has been maintained. The isotropy of the viscosity has been restored by applying different relaxation rates to different second order cumulants. It was confirmed that the method maintained a correct viscosity with second order convergence. The proposed methodology overcomes the stability problems of BGK CO for low values of viscosity, allowing for the correct simulation of natural phenomena (such as propagation of floods, dam breaks) that involve the propagation of water. Studying the breaking dam example, it was also confirmed that the new approach compares favorable to the classical BGK approach. It is possible to conclude that the cumulant CO is a promising tool to overcome issues of the BGK model: its higher stability properties make it more suitable for numerical simulation of shallow water equations. Since our approach is based on different relaxation rates for different cumulants it cannot be implemented within a single relaxation time BGK framework. However, the mechanism to sustain isotropy used in the BGK method can be implemented also in a MRT cascaded framework, based on central moments, as has recently be done by De Rosis[26]. His method is consistent with the BGK operator, as the latter is recovered exactly if all the moments relax with a common frequency. In the cumulant framework the two methods can even be combined[44] which provides an additional degree of freedom to further improve stability and/or accuracy.

List of acronyms

LBM: Lattice Boltzmann Method
SWE: Shallow Water Equations
LB SW: Lattice Boltzmann Shallow Water
CO: Collision Operator
SRT: Single Relaxation Time
MRT: Multi Relaxation Time
BGK: Bhatnagar- Gross- Krook
CumLB model: Cumulant Lattice Boltzmann Model
BGK SW model: BGK Shallow Water Model

PDF: Particle Distribution Function
D2Q9: Two-dimensional lattice pattern with 9 speed directions

ACKNOWLEDGMENTS

This work was supported by the Italian Ministry of Education, University and Research under PRIN grant No. 20154EHYW9 "Combined numerical and experimental methodology for fluid structure interaction in free surface flows under impulsive loading".

Conflict of interest

The authors declare no potential conflict of interests.

References

1. Krafczyk M, Tölke J, Luo LS. Large-eddy simulations with a multiple-relaxation-time LBE model. *International Journal of Modern Physics B.* 2003;17(01n02):33–39.

2. Far EK, Geier M, Kutscher K, Krafczyk M. Simulation of micro aggregate breakage in turbulent flows by the cumulant lattice Boltzmann method. *Computers & Fluids.* 2016;140:222–231.

3. Falcucci G, Ubertini S, Succi S. Lattice Boltzmann simulations of phase-separating flows at large density ratios: the case of doubly-attractive pseudo-potentials. *Soft Matter.* 2010;6(18):4357–4365.

4. Falcucci G, Ubertini S, Bella G, De Maio A, Palpacelli S. Lattice Boltzmann modeling of diesel spray formation and break-up. *SAE International Journal of Fuels and Lubricants.* 2010;3(2010-01-1130):582–593.

5. Ubertini S, Bella G, Succi S. Lattice Boltzmann method on unstructured grids: Further developments. *Phys. Rev. E.* 2003;68:016701.

6. Di Francesco S, Zarghami A, Biscarini C, Manciola P. Wall roughness effect in the lattice Boltzmann method. *AIP Conference Proceedings.* 2013;1558(1):1677-1680.

7. Yang X, Mehmani Y, Perkins WA, et al. Intercomparison of 3D pore-scale flow and solute transport simulation methods. *Advances in water resources.* 2016;95:176–189.

8. Zarghami A, Di Francesco S, Biscarini C. Porous substrate effects on thermal flows through a REV-scale finite volume lattice Boltzmann model. *International Journal of Modern Physics C.* 2014;25(02):1350086.

9. Di Francesco S, Biscarini C, Manciola P. Characterization of a flood event through a sediment analysis: The Tescio River case study. *Water.* 2016;8(7):308.

10. Biscarini C, Di Francesco S, Ridolfi E, Manciola P. On the Simulation of Floods in a Narrow Bending Valley: The Malpasset Dam Break Case Study. *Water.* 2016;8(11):545.

11. Qian YH, d'Humières D, Lallemand P. Lattice BGK Models for Navier-Stokes Equation. *EPL (Europhysics Letters).* 1992;17(6):479.

12. d'Humières D. Generalized lattice-Boltzmann equations. *Progress in Astronautics and Aeronautics.* 1994;159:450–450.

13. Geier M, Schönherr M, Pasquali A, Krafczyk M. The cumulant lattice Boltzmann equation in three dimensions: Theory and validation. *Computers & Mathematics with Applications.* 2015;70(4):507–547.

14. Krafczyk Manfred, Kucher Kostyantyn, Wang Ying, Geier Martin. DNS/LES Studies of Turbulent Flows Based on the Cumulant Lattice Boltzmann Approach. In: :519–531; 2015.

15. Geier M. *Ab initio derivation of the cascaded Lattice Boltzmann Automaton.* PhD Thesis, Albert-Ludwigs University Freiburg; 2006.

16. Biscarini C, Di Francesco S, Manciola P. CFD modelling approach for dam break flow studies. *Hydrology and Earth System Sciences.* 2010;14(4):705–718.

17. Salmon Rick. The lattice Boltzmann method as a basis for ocean circulation modeling. *Journal of Marine Research.* 1999;57(3):503–535.

18. Dellar PJ. Non-hydrodynamic modes and a priori construction of shallow water lattice Boltzmann equations. *Physical Review E - Statistical, Nonlinear, and Soft Matter Physics.* 2002;65(3).

19. Zhou JG. *Lattice Boltzmann Methods for Shallow Water Flows*. Springer-Verlag; 2004.

20. Thommes G, Seaid M, Banda MK. Lattice Boltzmann methods for shallow water flow applications. *Int. J. Numer. Methods Fluids.* 2007;55(7):673–692.

21. Shafiai SH. *Lattice Boltzmann method for simulating shallow free surface flows involving wetting and drying.* PhD Thesis, University of Liverpool; 2011.

22. Pietro P, Sciortino G., La Rocca M. On the effect of the intrinsic viscosity in a two-layer shallow water lattice Boltzmann model of axisymmetric density currents. *Journal of Hydraulic Research.* 2013;51(6):668-680.

23. Bhatnagar PL, Gross EP, Krook M. A Model for Collision Processes in Gases. I. Small Amplitude Processes in Charged and Neutral One-Component Systems. *Phys. Rev.*. 1954;94:511–525.

24. Peng Y. *Lattice Boltzmann Simulations of Environmental Flow Problems in Shallow Water Flows.* PhD Thesis, University of Liverpool; 2012.

25. Liu H. *Lattice Boltzmann Simulations for Complex Shallow Water Flows.* PhD Thesis, University of Liverpool; 2009.

26. De Rosis A. A central moments-based lattice Boltzmann scheme for shallow water equations. *Comput. Methods Appl. Mech. Engrg.*. 2017;319:379–392.

27. Toro E. *Shock-capturing methods for free-surface shallow flows*. John Wiley New York; 2001.

28. Wolf-Gladrow DA. Lattice-gas cellular automata and lattice Boltzmann models: an introduction. In: Springer 2004.

29. Cambridge University. *Lattice Planes and Miller Indices.* https://www.doitpoms.ac.uk/tlplib/miller_indices/index.php; 2008.

30. Geier Martin, Pasquali Andrea. Fourth order Galilean invariance for the lattice Boltzmann method. *Comput. Fluids.* 2018;166:139–151.

31. Geveler M, Ribbrock D, Göddeke D, Turek S. Lattice-boltzmann simulation of the shallow-water equations with fluid-structure interaction on multi-and manycore processors. In: :92–104Springer Berlin/Heidelberg; 2011.

32. Frandsen JB. A simple LBE wave runup model. *Progress in Computational Fluid Dynamics, An International Journal.* 2008;8(January 2008):222.

33. Chen S, Doolen GD. Lattice Boltzmann method for fluid flows. *Annual review of fluid mechanics.* 1998;30(1):329–364.

34. Altmann C, Beck A, Birkefeld A, et al. Discontinuous Galerkin for High Performance Computational Fluid Dynamics. In: Springer 2013 (pp. 225–238).

35. Krüger T, Varnik F, Raabe D. Second - order convergence of the deviatoric stress tensor in the standard Bhatnagar - Gross - Krook lattice Boltzmann method. *Physical Review E - Statistical, Nonlinear, and Soft Matter Physics.* 2010;82(2):025701.

36. Dubois F, Lallemand P. Quartic parameters for acoustic applications of lattice Boltzmann scheme. *Computers & Mathematics with Applications.* 2011;61(12):3404–3416.

37. Geier M, Pasquali A, Schönherr M. Parametrization of the cumulant lattice Boltzmann method for fourth order accurate diffusion part I: Derivation and validation. *Journal of Computational Physics.* 2017;348:862–888.

38. d'Humières Dominique, Ginzburg Irina. Viscosity independent numerical errors for Lattice Boltzmann models: from recurrence equations to "magic" collision numbers. *Computers & Mathematics with Applications.* 2009;58(5):823–840.

39. Stoker J. J.. *WATER WAVES The Mathematical Theory With Applications*. Wiley-Interscience, New York; 1957.

40. Delestre O, Lucas C, Ksinant PA, et al. SWASHES: a compilation of shallow water analytic solutions for hydraulic and environmental studies. *International Journal for Numerical Methods in Fluids.* 2013;72(3):269–300.

41. Arfken G B, Weber H J. *Mathematical methods for physicists*. Academic Press New York; 1972.

42. Fennema Robert J, Chaudhry M Hanif. Explicit methods for 2-D transient free surface flows. *Journal of Hydraulic Engineering*. 1990;116(8):1013–1034.

43. Murillo Javier, García-Navarro P. Weak solutions for partial differential equations with source terms: Application to the shallow water equations. *Journal of Computational Physics.* 2010;229(11):4327–4368.

44. Venturi S. *Lattice Boltzmann shallow water equations for large scale hydraulic analysis.* PhD Thesis, University of Florence, Pisa, Perugia and Technische Universität Braunschweig; 2018.

How to cite this article: Venturi S., S. Di Francesco, M. Geier, and P. Manciola (2019), A new collision operator for lattice Boltzmann shallow water model: a convergence and stability study, ..., ...

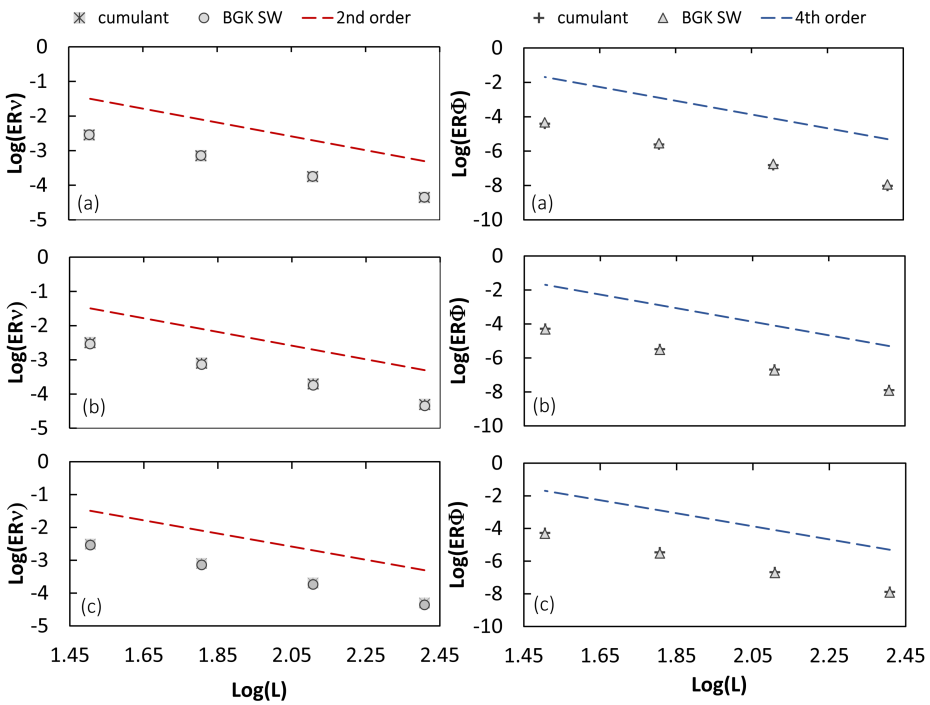

FIGURE 1 Shear wave test. Comparison of normalized error in viscosity ER_ν and phase lag ER_Φ, for the three viscosities: ν=(a) 0.01, 0.001 (b), 0.0001 (c), h=1. Values in l.u.

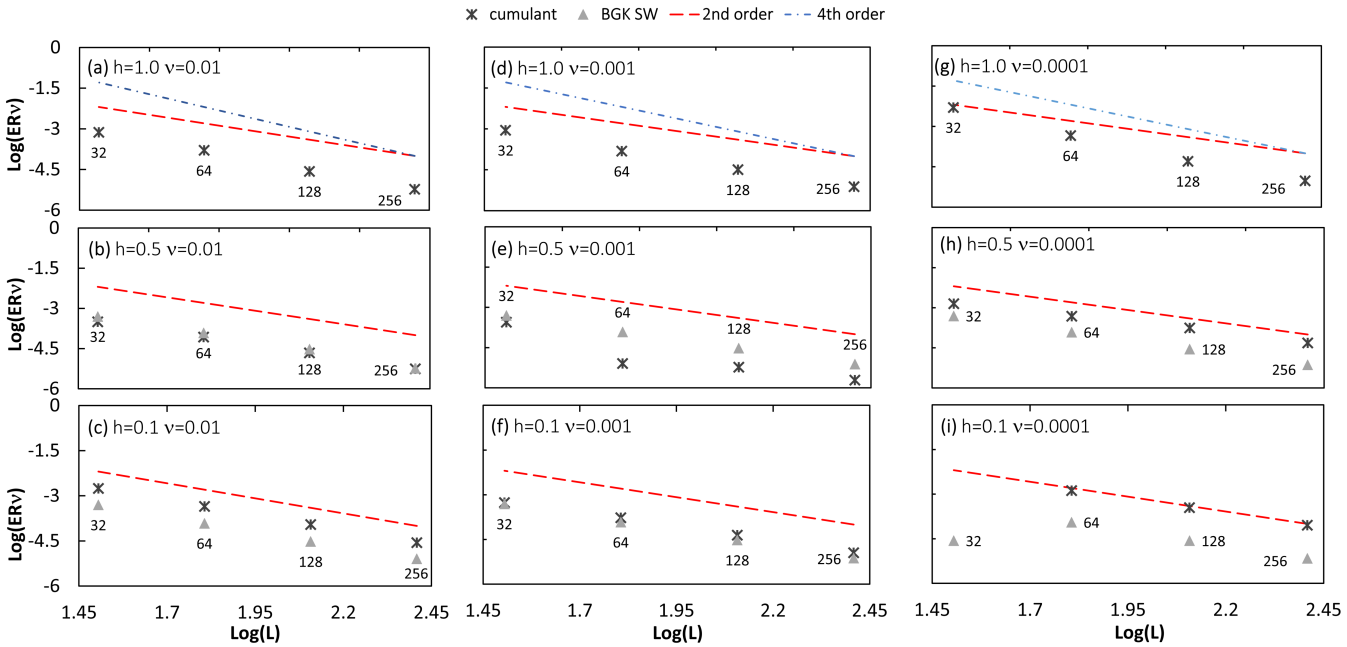

FIGURE 2 Taylor Green Vortex test. Slow velocity set - comparison of normalized error in viscosity ER_ν, for the three depths: h=1.0 , 0.5 , 0.1 and viscosities: ν=0.01, 0.001, 0.0001. The label shows the different values of the domain width L. Values in l.u.

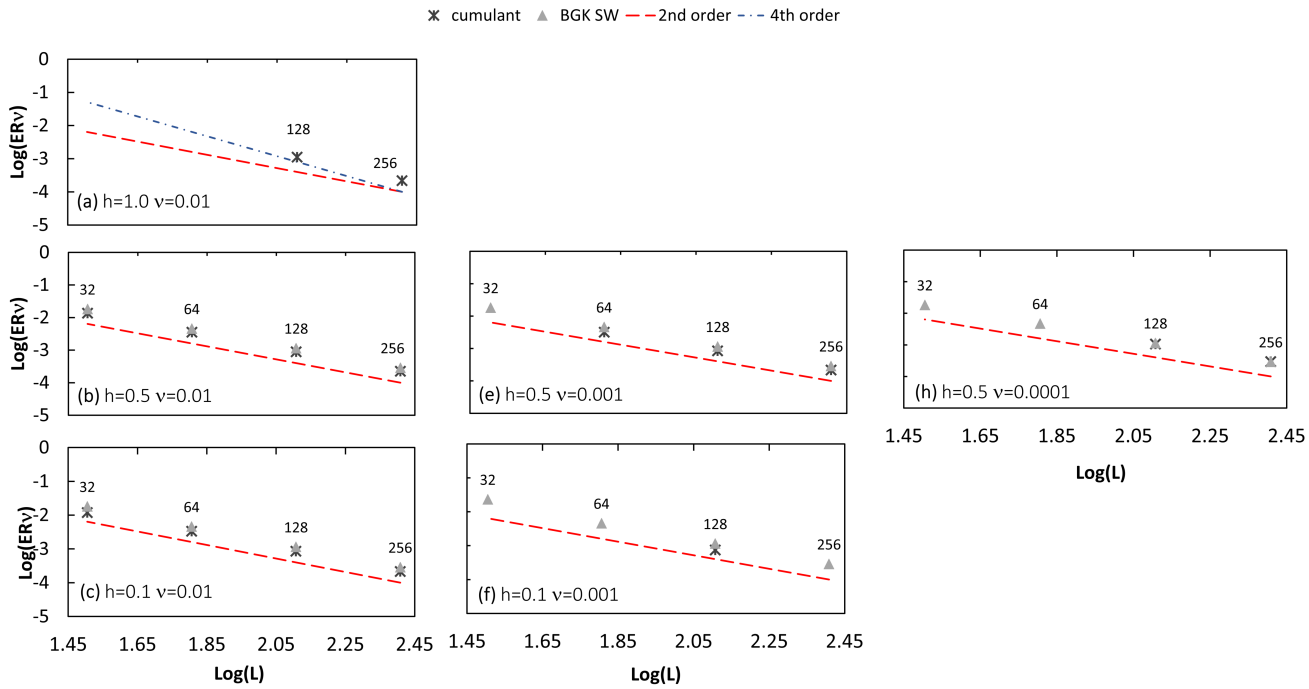

FIGURE 3 Taylor Green Vortex test. Fast velocity set - comparison of normalized error in viscosity ER_ν, for the three depths: h=1 (a), 0.5 (b), 0.1 (c) and viscosities: ν=0.01, 0.001, 0.0001. The label shows the different values of the domain width L. Values in l.u.

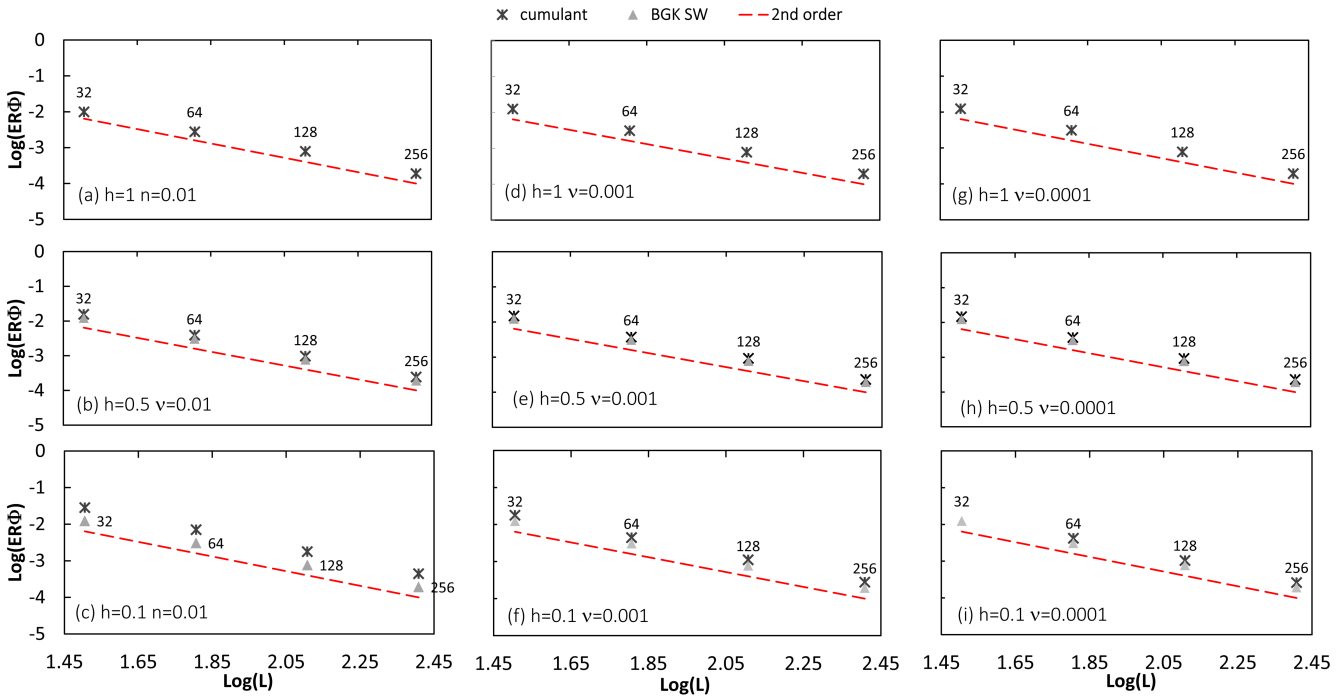

FIGURE 4 Taylor Green Vortex test. Slow velocity set - phase lag ER_Φ, for the three depths: h=1.0 , h=0.5 , h=0.1 - ν=0.01, 0.001, 0.0001. The label shows the different values of the domain width L. Values in l.u.

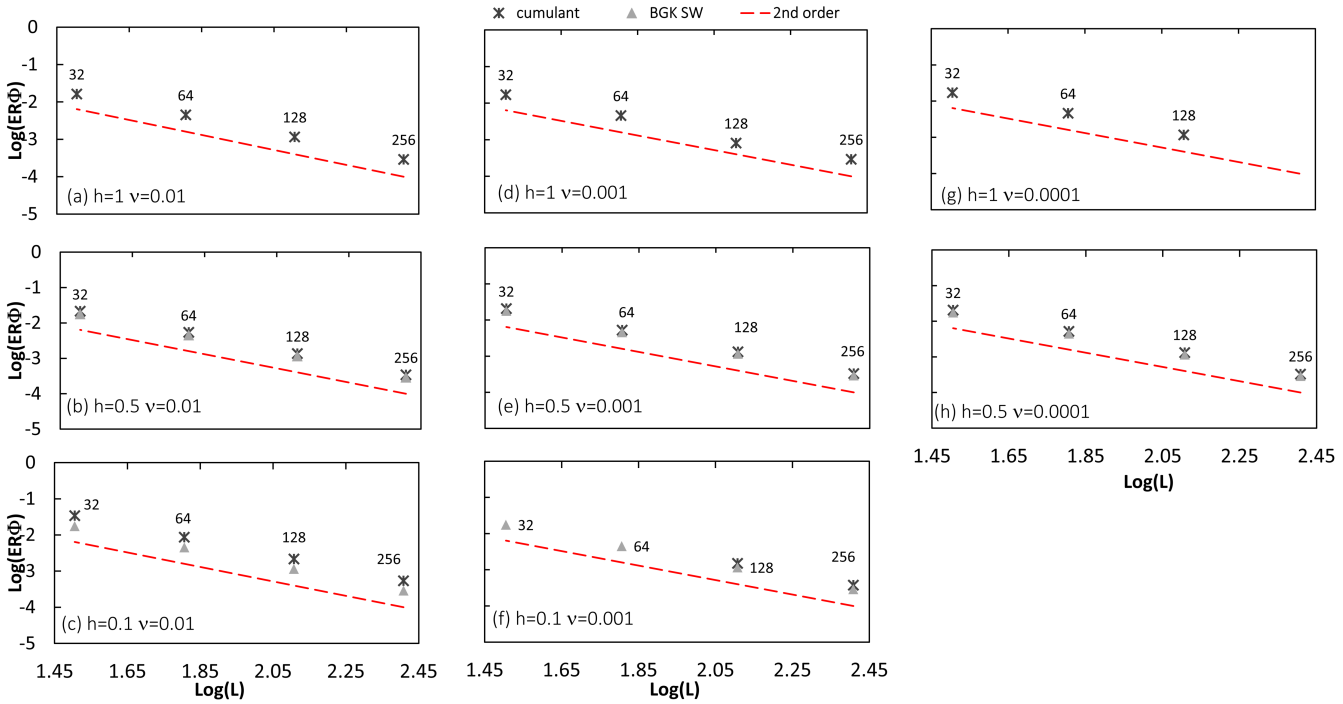

FIGURE 5 Taylor Green Vortex test. Fast velocity set - phase lag ER_Φ, for the three depths: h=1.0 , h=0.5 , h=0.1 - ν=0.01, 0.001, 0.0001. The label shows the different values of the domain width L. Values in l.u.

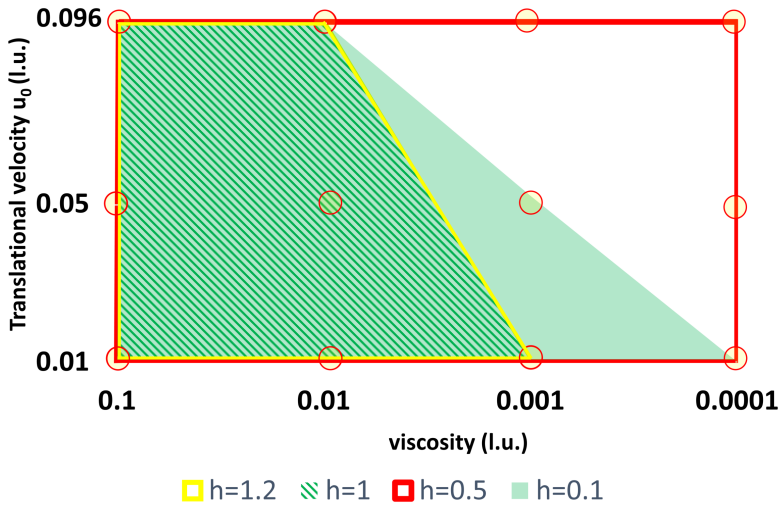

FIGURE 6 Stability range - cumulant model with the variation of viscosity and translational velocity (l.u.).

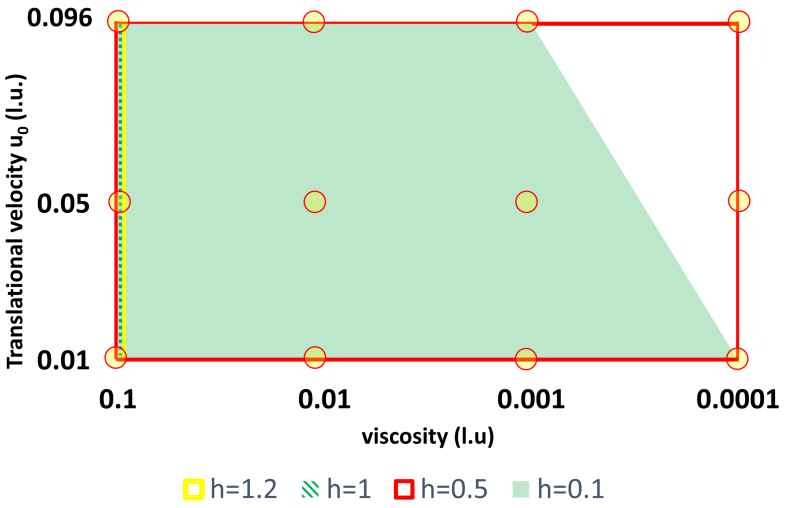

FIGURE 7 Stability range - BGK SW model with the variation of viscosity and translational velocity (l.u.).

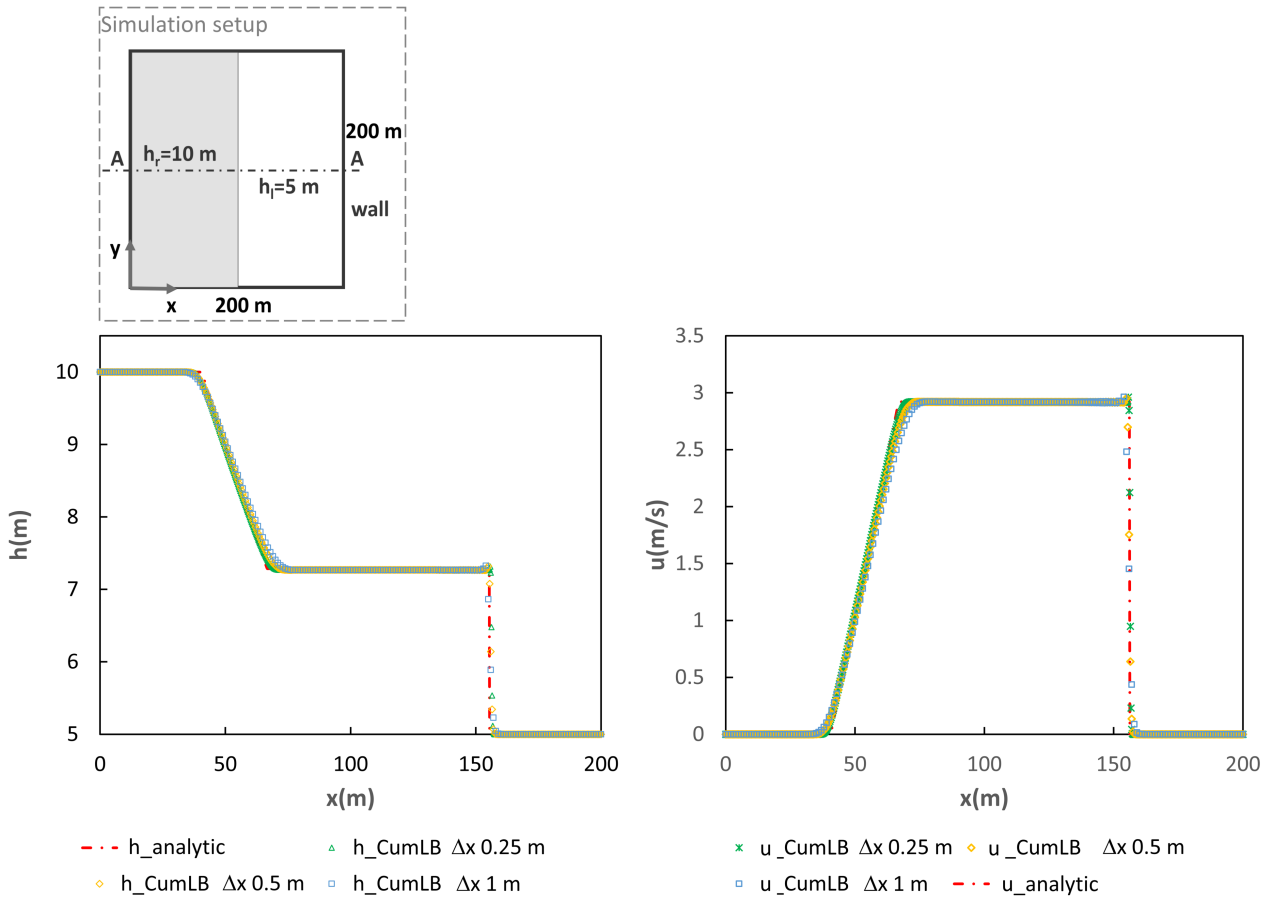

FIGURE 8 Stoker Dam Break test case. Top: simulation setup. Bottom: CumLB model - water depth h (m) and velocity u (m/s) at section A - A for different grid spacing.

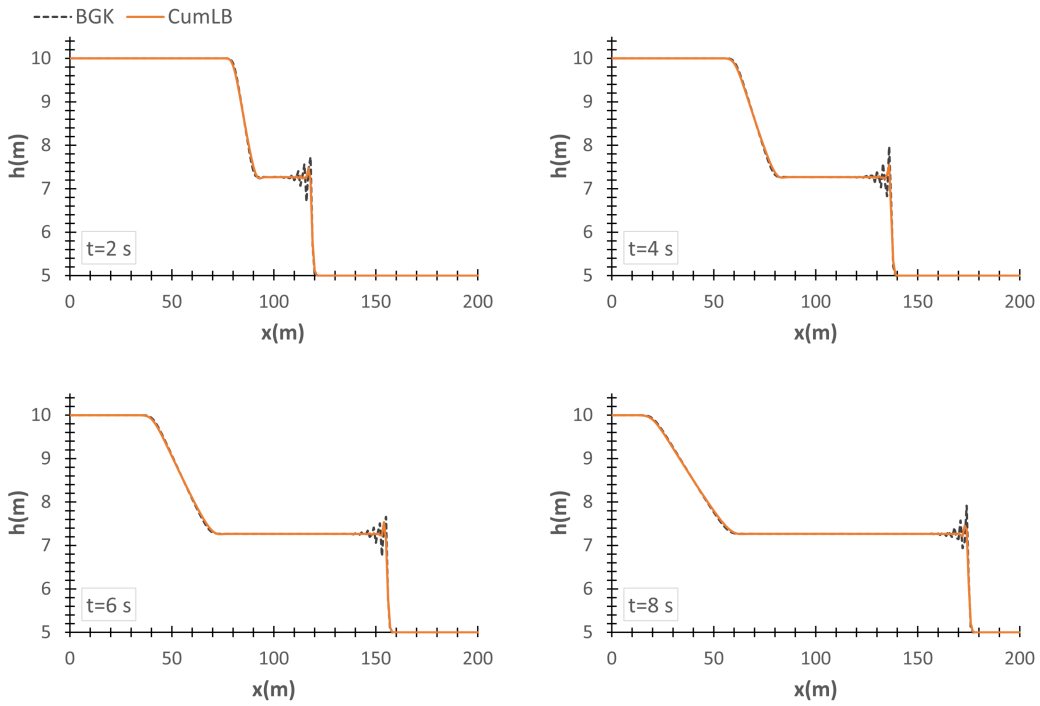

FIGURE 9 Stoker Dam Break - water depth h (m): comparison for CumLB and BGK SW models at time t=2, 4, 6, 8 s. Δx=1m.

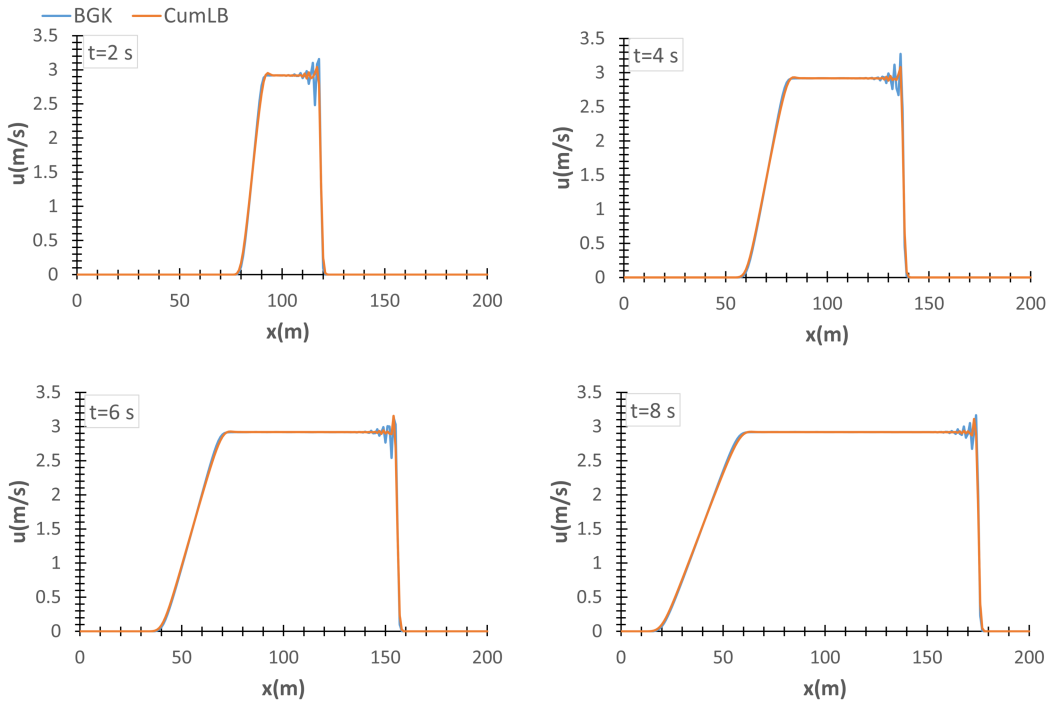

FIGURE 10 Stoker Dam Break - water depth u (m/s): comparison for CumLB and BGK SW models at time t=2, 4, 6, 8 s. Δx=1m.

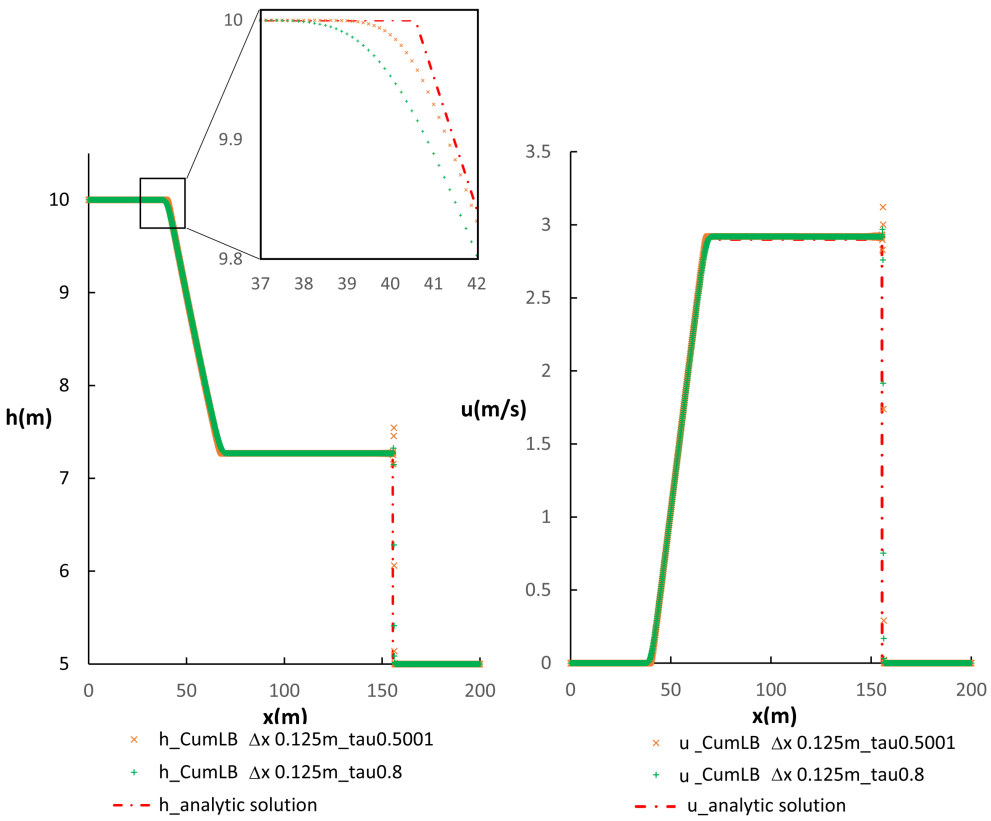

FIGURE 11 Stoker Dam Break - water depth h (m) and velocity u (m/s) for τ=0.5001 and τ=0.8 (CumLB) and analytical solution at time t=6 s. Δx=0.125 m.

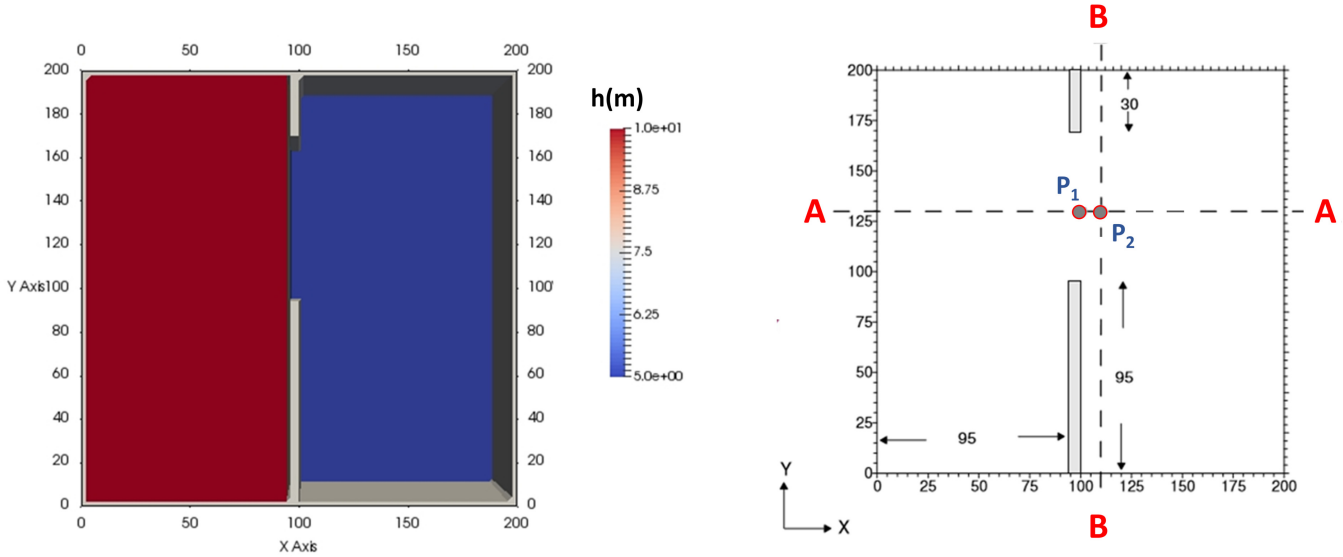

FIGURE 12 Simulation setup. On the left, the water depth h in the domain. On the right, the position of the sections A-A and B-B and of the P_1 and P_2 points. Measures in meters.

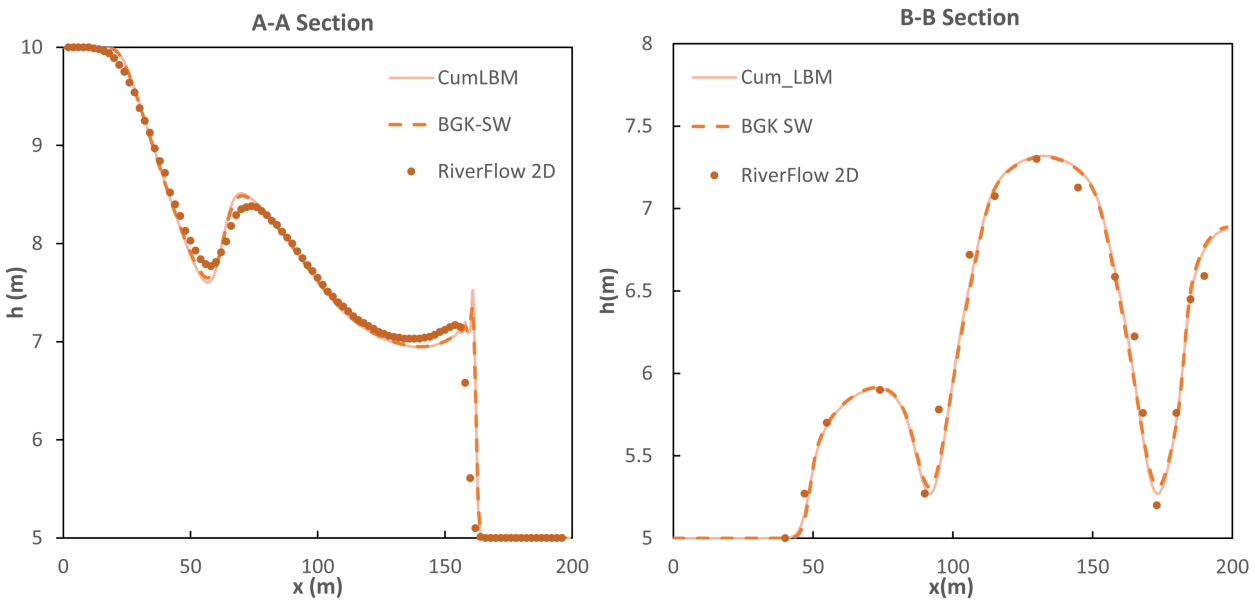

FIGURE 13 Longitudinal (A-A) and transversal (B-B) sections in dam-break domain. Comparison of the water depth (h) values at 7.2 s for different models: CumLB, BGK-SW and RiverFlow 2D.

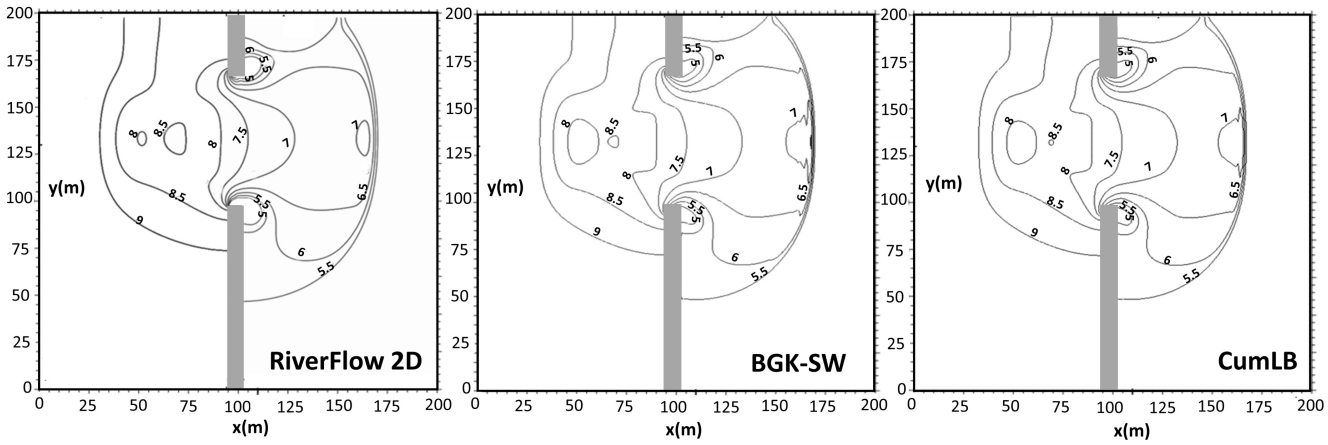

FIGURE 14 Water depth (h) contours level for different models: RiverFlow 2D, BGK-SW and CumLB model.

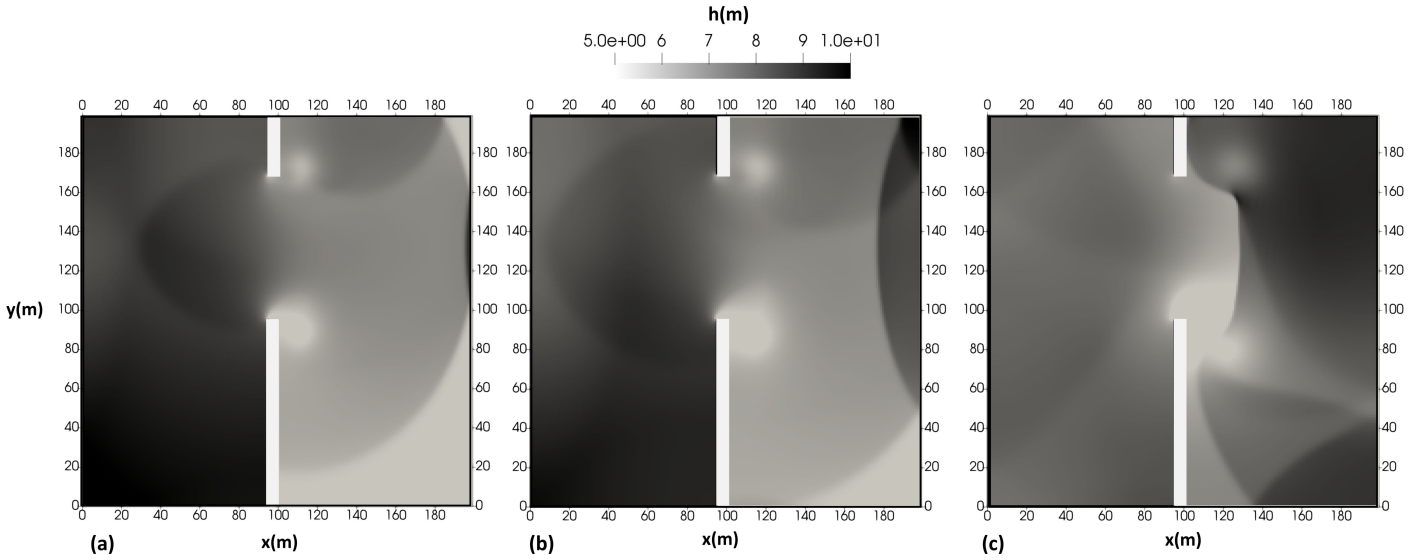

FIGURE 15 CumLB model: water depth (h) level for different times: 11.5 s (a); 14 s (b); 23.3 s (c).

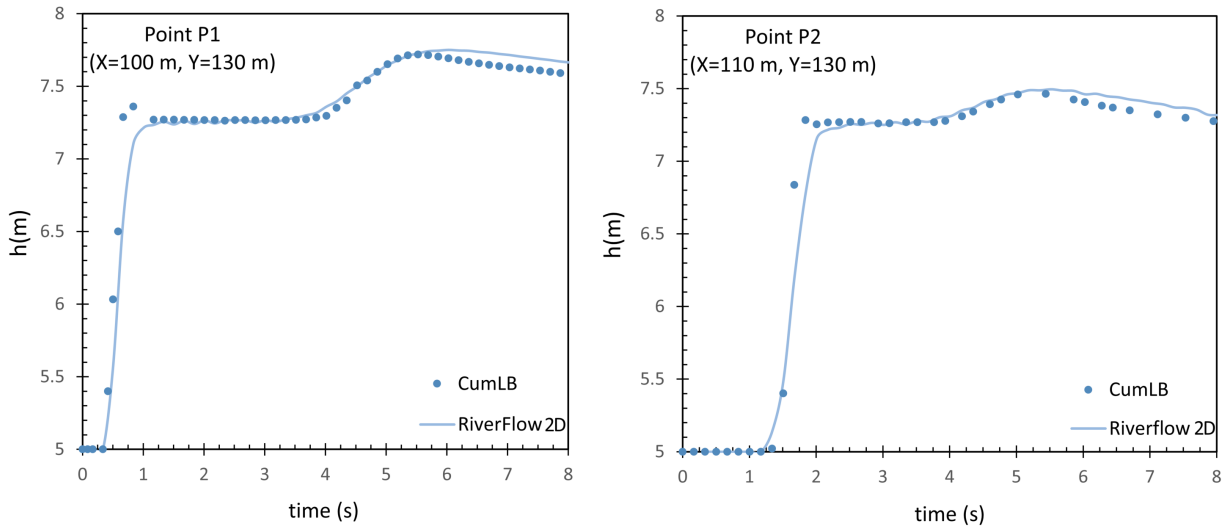

FIGURE 16 Comparison of water depth hydrographs at points P1 and P2, CumLB model and RiverFlow 2D model.